Preparation and characterization of a porous silicate material from silica fume

Yinmin Zhang[†], Haiping Qi, Yaqiong Li, Yongfeng Zhang, and Junmin Sun

College of Chemical Engineering, Inner Mongolia University of Technology, Hohhot, 010051 China

Abstract−A porous silicate material derived from silica fume was successfully prepared and characterized by X-ray diffraction (XRD), X-ray photoelectron spectroscopy (XPS), Fourier-transform infrared (FT-IR) spectroscopy, Thermogravimetry and Differential thermal gravity (TG-DTG), N_2 adsorption and desorption isotherms, and scanning electron microscopy (SEM). Raw silica fume was analyzed by XRD, FT-IR and SEM. The analysis results of silica fume indicated that SiO_2 in silica fume is mainly determined as amorphous state, and that the particles of raw silica fume exhibited characteristic spherical structure with a diameter of from 50 nm to 200 nm. The preparation of the porous silicate material involved two steps. The first step was the extraction of the SiO_3^{2-} leachate from raw silica fume. The maximum value of SiO_3^{2-} extraction yield was obtained under the following conditions: reaction temperature of 120 $^{\circ}$C, reaction time of 120 min, NaOH concentration of 15%, and alkali to SiO_2 molar ratio of 2. The second step was the preparation of the porous silicate material though the reaction of SiO_3^{2-} leachate and $Ca(OH)_2$ suspension liquid. The optimum preparation conditions were as follows: preparation temperature of 90 $^{\circ}$C, preparation time of 1.5 h, Si/Ca molar ratio of 1 : 1, and stirring rate of 100 r/min. The BET surface area and pore size of the porous silicate material were 220.7 $m^2 \cdot g^{-1}$ and 8.55 cm^3/g, respectively. The porous silicate material presented an amorphous and unordered structure. The spectroscopic results indicated that the porous silicate material was mainly composed of Si, Ca, O, C, and Na, in the form of Ca^{2+}, SiO_3^{2-}, CO_3^{2-} and Na^+ ions, respectively, which agreed with the XRD, TG-DSC, and FT-IR data. The N_2 adsorption-desorption isotherm mode indicates that the porous silicate material belonged to a typical mesoporous material. The porous silicate material presented efficiency for the removal of formaldehyde: it showed a formaldehyde adsorption capacity of 8.01 mg/g for 140 min at 25 $^{\circ}$C.

Keywords: Silica Fume, Porous Silicate Material, Preparation, Mesoporous Material

INTRODUCTION

Silica fume, also known as microsilica or condensed silica fume, is a byproduct formed by the rapid condensation of volatile SiO_2 and Si gases in the production of ferrosilicon alloy and industrial silicon [1,2]. Silica fume is mainly composed of SiO_2, and contains small amounts of CaO, MgO, K_2O, Fe_2O_3, free carbon and other impurities [3-6]. The color of silica fume varies from white to dark gray as the content of Fe_2O_3 and free carbon increases, and the content of SiO_2 dictates the quality grade of silica fume [7]. The particle size range of silica fume is approximately 0.15-0.3 μm [2]. In recent years, the output of silica fume has significantly increased with the number of ferrosilicon and industrial silicon furnaces, especially in China [8]. Silica fume processes a large number of accumulations not only because of the development of ferrosilicon alloy and industrial silicon, but also because of the generation of low quality grade silica fume. The accumulation of silica fume occupies enormous tracts of farmland, destroys the ecology, and causes harm to human health because of its fine particle size. Therefore, the resource recovery of silica fume has become an important research topic in the world, especially in China. Currently, silica fume has been used in the cement, concrete, rubber, fireproof material, coating, and met-

allurgy, among others [3,9-14]. However, the above application fields have strict requirements for silica fume quality grade. The cement and concrete industry requires >85% SiO_2 content in silica fume, and fireproof material, coating and rubber fields requirement higher silica fume quality grade (SiO_2 wt% >90%). Currently, the silica fume with the content of SiO_2 wt% less than 90% does not have application value as the development of technology in various fields. Hence, the resource utilization of low grade silica fume (SiO_2 wt% ≤85%) has been an important problem in the ferrosilicon alloy and industrial silicon filed. In general, the application of low grade silica fume has been focused on traditional construction materials, including pottery, cement and brick [1-3], which belong to low value added application methods in China. Therefore, it is of great importance to study efficient, high value and innovative approaches for the resource recovery of silica fume.

In this work, we propose a innovative and facile approach of silica fume application; and a porous silicate material derived from silica fume was hydrothermally synthesized and characterized by X-ray diffraction (XRD), X-ray photoelectron spectroscopy (XPS), Fourier-transform infrared (FT-IR) spectroscopy, thermogravimetry and differential scanning calorimetry (TG-DSC), N_2 adsorption and desorption isotherms, and scanning electron microscopy (SEM). The porous silicate material has potential applications in polymer material, papermaking industry and adsorption field. Further work is being carried out in our research group. The study might lead to a breakthrough in the field of silica fume resource

[†]To whom correspondence should be addressed.
E-mail: pzqm163@163.com

Table 1. The chemical composition of raw silicate fume (wt%)

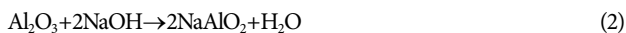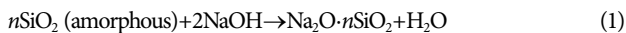| Composition	SiO_2	MgO	K_2O	CaO	Fe_2O_3	NaO	Al_2O_3	Mass loss
Raw silicate powder	81.94	3.79	3.17	1.85	1.66	0.82	0.63	4.5

recovery and utilization for high value.

EXPERIMENTAL

1. Material

Silicate fume was obtained from Ordos Metallurgical Group Co., Ltd. (Ordos, China). The chemical composition of the sample is 81.94 wt% SiO_2 and other components (Table 1). NaOH of 97.0-99.9 wt% purity and CaO was supplied by Sinopharm Chemical Reagent Co., Ltd. Deionized water was prepared in laboratory.

2. SiO_3^{2-} Extraction from Raw Silica Fume

Silicate fume was calcined at 200-300 °C for 2-3 h to remove carbonaceous components (defined as calcined silica fume, CSP). CSP was reacted with a 10%-35% NaOH solution at 80-160 °C. The molar ratios of alkali to SiO_2 in CSP were 1.0, 1.5, 2.0, 2.5, 3.0, and 3.5. The suspension liquid was stirred for 30-180 min, filtered, and then washed to obtain the leachate. The main chemical reaction in the method is shown in formula (1), and the side reaction is shown in formula (2).

$$nSiO_2 \text{ (amorphous)} + 2NaOH \rightarrow Na_2O \cdot nSiO_2 + H_2O \quad (1)$$

$$Al_2O_3 + 2NaOH \rightarrow 2NaAlO_2 + H_2O \quad (2)$$

In this method, the molar concentration of the obtained leachate was analyzed using silico-fluoride natrium volumetry method [15, 16]. The reaction conditions, including reaction temperature, T_1, reaction time, t_1, concentration of NaOH, w, and the mass ratio of CSP/alkali, R, were investigated. The SiO_3^{2-} extraction yield was calculated using formula (2):

$$E(SiO_3^{2-}) = M(SiO_3^{2-}) \times V/M_s \quad (2)$$

where $E(SiO_3^{2-})$ is the SiO_3^{2-} extraction yield in %, $M(SiO_3^{2-})$ is the SiO_3^{2-} concentration in the obtained leachate in g/L, V is the leachate volume in L, and M_s is the SiO_2 mass in the calcined silica fume in g.

3. Preparation of Porous Silicate Material

The above obtained SiO_3^{2-} leachate (1 mol/L) was mixed with $Ca(OH)_2$ suspension liquid, and the liquid mixture was reacted at 30-130 °C for 0.5-3 h under stirring. Then, the liquid mixture was filtered and washed three times with deionized water. The obtained filter cake was dried at 100-120 °C to obtain the porous silicate material. In this process, the reaction conditions, including reaction time t_2, reaction temperature T_2, SiO_3^{2-} to $Ca(OH)_2$ molar ratio (Si/Ca), and stirring rate on the Brunauer-Emmett-Teller (BET) surface area of the porous silica material were investigated. A schematic of the apparatus and the entire flow diagram of the experiment are shown in Fig. 1 and Fig. 2, respectively.

4. Models

Langmuir isotherm model was used to investigate the adsorption equilibrium of porous silicate material for formaldehyde. The linear form of Langmuir isotherm equation is represented by the
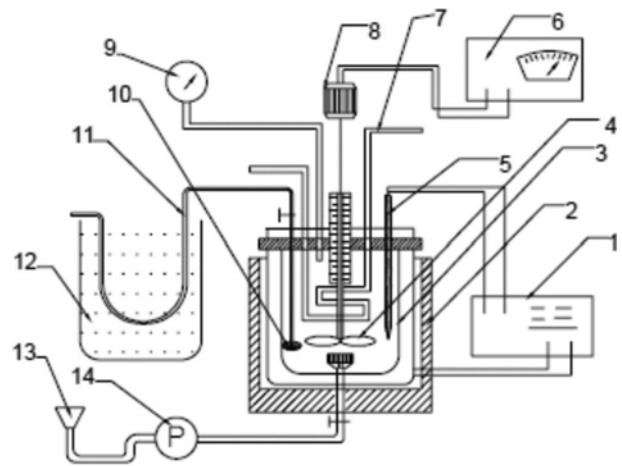

Fig. 1. Schematic diagram of experimental apparatus [2].

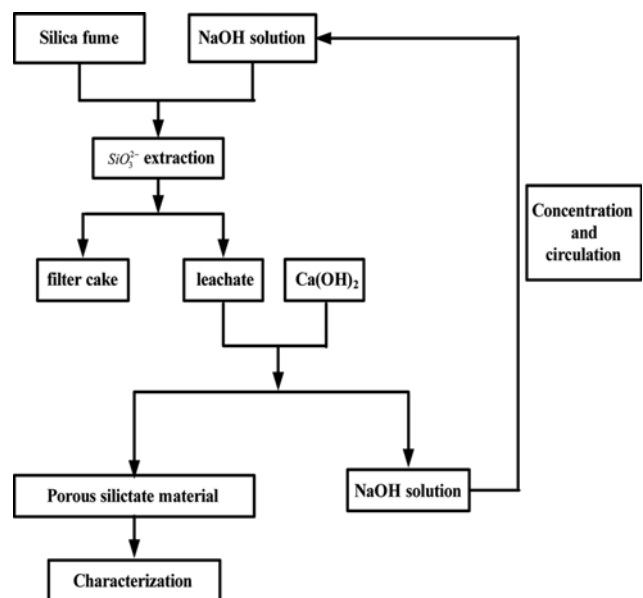|	
1. Thermostat	8. Motor
2. Insulating layer	9. Pressure gage
3. Reactor	10. Filter cloth
4. Stiming paddle	11. Probe tube
5. Thermocouple	12. Cooling water
6. Speed controller	13. Solution feeding trough
7. Condenser system	14. Liquid pump

Fig. 2. The whole flow diagram of experimental.

following equation:

$$\frac{Ce}{q_e} = \frac{1}{q_{max}} \times \frac{1}{K_L} + \frac{Ce}{q_{max}}$$

where Ce is the mass concentration of formaldehyde at adsorption equilibrium, mg/L; q_e is the adsorption capacity of porous sili-

cate material at adsorption equilibrium, mg/g; K_L is the Lagrange constant; q_{max} is the theoretical maximum adsorption capacity. The value of Ce/q_e was in agreement with the K_L according to the previous reference [17-19].

5. Characterization

The chemical composition of silicate fume was obtained using an X-ray fluorescence analyzer spectrometer. The XRD patterns of the prepared samples were performed using a Rigaku D/max 2500PC powder X-ray diffractometer operated at 40 kV and 150 mA. Cu $K\alpha$ radiation with 15.40596 nm was used. The scanning step size was 0.02°, and the slit width: DS=SS=1°, RS=0.3 mm. Measurements were performed in the range 2.6-60° in 2θ with the scanning rate of 2°/min. FT-IR spectroscopy was conducted using a Fourier transform infrared spectrometer (Magna-IR 750 Nicolet) at a resolution of 4 cm^{-1} in the 4,000-400 cm^{-1} region. A total of 32 scans were accumulated. The samples were prepared on potassium bromide (KBr) pellets (ca. 2% by mass in KBr). The morphology of the prepared samples was characterized via electron microscopy (SEM) with a S4800 low-temperature-field emission electron microscope (Rigaku Co.). X-ray photoelectron spectroscopy (XPS) data of the porous silicate material were obtained with an ESCLAB-250Xi photoelectron spectrometer (Thermo-Fisher Co., America).

RESULTS AND DISCUSSION

1. Characterization of Raw Silica Powder

As shown in Fig. 3, the XRD pattern of raw silica fume shows two dispersing and wide diffraction peaks at 2θ=18°-22° and 2θ= 28°-34°. The result indicates that SiO$_2$ is generally in amorphous state, which is attributed to the rapid condensation of volatile SiO$_2$ and Si gases and to the surface tension in the phase-transition [2]. However, the sharp diffraction peak with the value of 0.34 nm at approximately 2θ=26° is attributed to quartz, which indicates that raw silica fume contains a small amount of crystalline silica.

FI-IR spectroscopy reveals information about the molecular structure of materials.

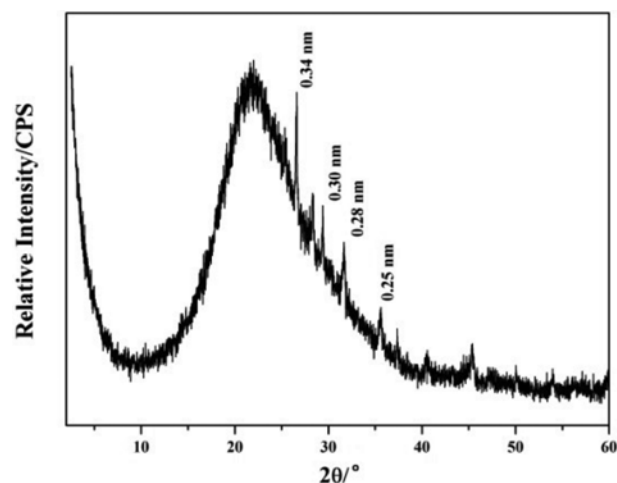Fig. 4 shows the FT-IR spectroscopy of raw silica fume. Silica

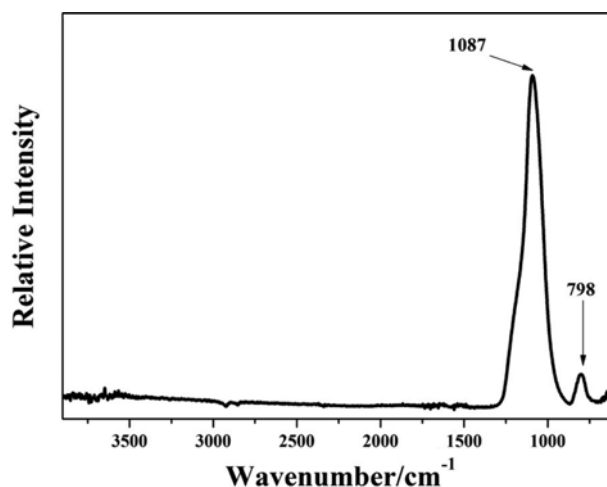Fig. 3. The XRD pattern of raw silicate powder.

Fig. 4. The FT-IR spectroscopy of raw silicate fume.

fume is mainly composed of amorphous silica. Two evident bands can be observed in the 500-1,500 cm^{-1} region. The intense band at
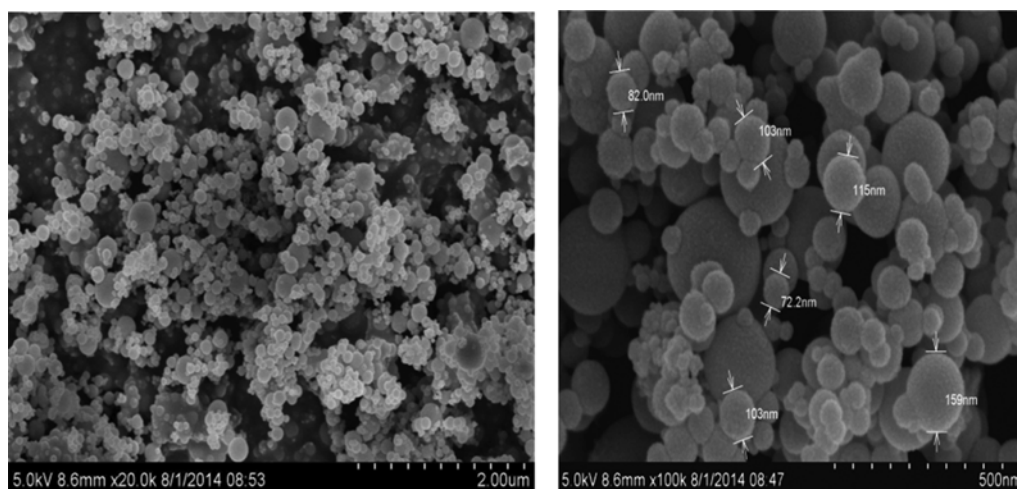

Fig. 5. The SEM images of raw silicate fume.

approximately 1,087 cm^{-1} is assigned to the stretching vibration mode of Si-O. The band at approximately 798 cm^{-1} is attributed to the bending vibration mode of Si-O [20].

SEM images of raw silica fume are shown in Fig. 5. The particles of raw silica fume exhibited characteristic spherical structure with the diameter of from 50 nm to 200 nm. Secondary particle aggregates were observed obviously, which is due to the surface tension between primary particles. The average distances between secondary particle aggregates ranged from dozens of nanometers to hundreds of nanometers.

2. Influence of Reaction Condition on SiO$_3^{2-}$ Extraction Yield

2-1. Influence of Reaction Temperature on SiO$_3^{2-}$ Extraction Yield

The influence of reaction temperature on SiO$_3^{2-}$ extraction yield was investigated under the following conditions: t$_1$=120 min, w= 15%, and R=2. The results are shown in Fig. 6(a). The SiO$_3^{2-}$ extraction yield gradually increased with increasing reaction temperature and reached the maximum SiO$_3^{2-}$ extraction yield of 90.69% at 120 °C. This result is reasonable because high temperatures strengthen the liquid-solid mass transfer and accelerate the reaction rate [21]. However, the SiO$_3^{2-}$ extraction yield decreased when the reaction temperature exceeded 120 °C. The results may be attributed to the volatilization of NaOH solution and the unstable temperature of the mixture, which weakened the solid-liquid reaction [22].

2-2. Influence of Reaction Time on SiO$_3^{2-}$ Extraction Yield

The influence of reaction time on SiO$_3^{2-}$ extraction yield was investigated under the following conditions: T$_1$=120 °C, w=15%, and R=2. and the results are shown in Fig. 6(b). As shown in Fig. 6(b), the SiO$_3^{2-}$ extraction yield gradually increased and reached the maximum value of 90.69% when the reaction time was extended to 120 min. The SiO$_3^{2-}$ extraction yield slightly decreased when the reaction time was further extended from 120 min to 180 min, possibly because of a side reaction in the suspension liquid. The results indicated that the reaction of amorphous SiO$_2$ with NaOH in suspension liquid was completed at 120 min.

2-3. Influence of NaOH Concentration on SiO$_3^{2-}$ Extraction Yield

The effects of different NaOH concentrations (10%, 15%, 20%, 25%, and 30%) on SiO$_3^{2-}$ extraction yield were studied under the following conditions: T$_1$=120 °C, t=120 min, and R=2. The results are shown in Fig. 6(c). The SiO$_3^{2-}$ extraction yield gradually increased when the NaOH concentration was increased from 10% to 15% and then sharply decreased when the NaOH concentration was further increased from 15% to 35%. The maximum extraction yield was 90.69% at 15% NaOH concentration.

2-4. Influence of Alkali-to-SiO$_2$ Molar Ratio on SiO$_3^{2-}$ Extraction Yield

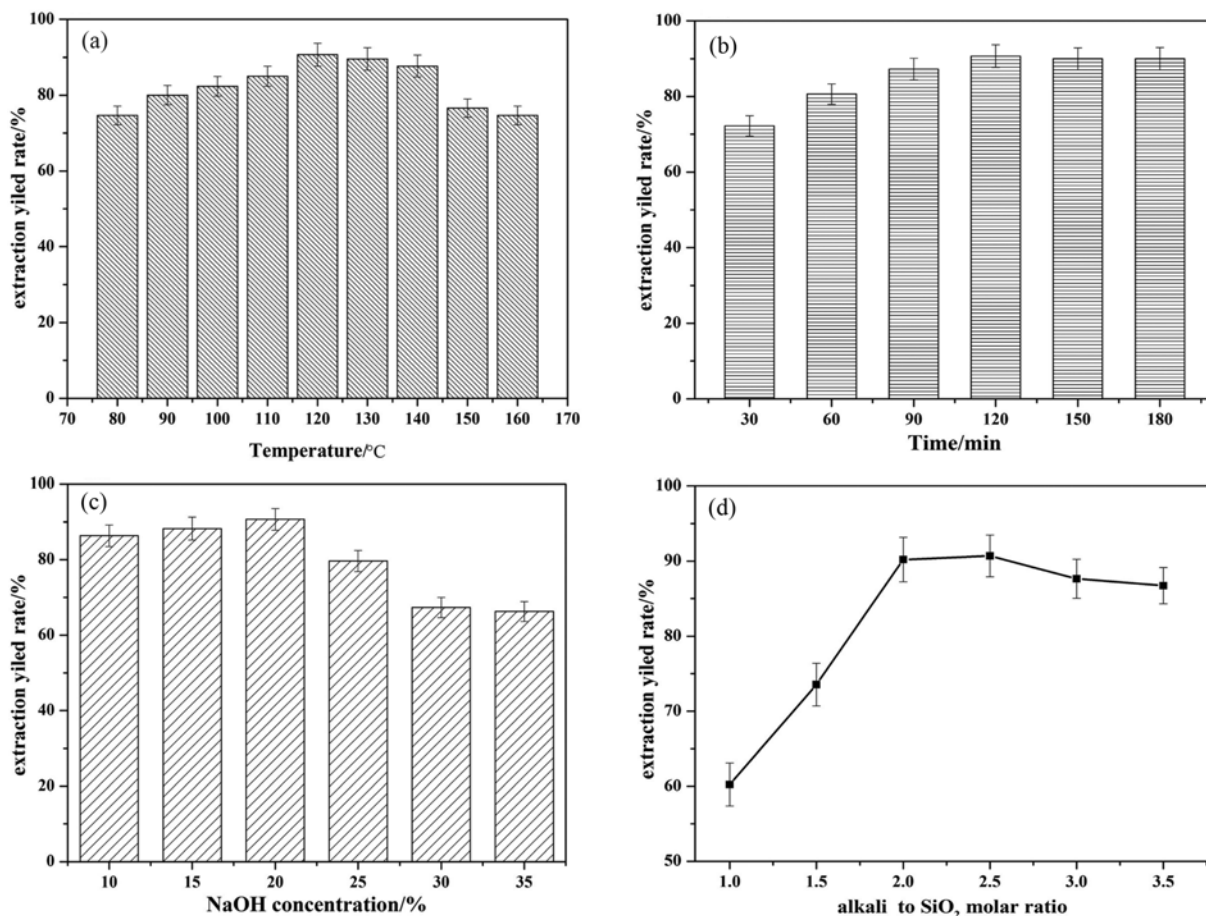The influence of alkali-to-SiO$_2$ molar (R) ratio on SiO$_3^{2-}$ extrac-

Fig. 6. (a) The effect of temperature on SiO$_3^{2-}$ extraction yield rate, (b) the effect of time on SiO$_3^{2-}$ extraction yield rate, (c) the effect of NaOH concentration on SiO$_3^{2-}$ extraction yield rate, (d) the effect of silicate powder to alkali mass ratio on SiO$_3^{2-}$ extraction yield rate.

tion yield was investigated under the following conditions: $T_1=$ 120 °C, t=120 min, and w=15%. The selected alkali-to-SiO$_2$ molar ratios (R) were 1.0, 1.5, 2.0, 2.5, 3.0, and 3.5. As shown in Fig. 6(d), the SiO$_3^{2-}$ extraction yield significantly increased with increasing R and reached the maximum of 90.69% when the R was 2.5. Then, the SiO$_3^{2-}$ extraction yield gradually decreased when the R exceeded 2.5. Moderate content of NaOH could make the reaction molecules contract fully and sufficiently complete the reaction [23]. However, excessive NaOH molecules may react with impurities (Fe$_2$O$_3$ and Al$_2$O$_3$), and the reaction product would further react with NaO·nSiO$_2$.

3. Influence of Preparation Conditions on the Porous Silicate Materials

3-1. Influence of Preparation Temperature and Time on the Porous Silicate Materials

The influence of preparation temperature on the BET surface area and pore volume of the silicate material is shown in Fig. 7(a). The BET surface area of the silicate material evidently increased with increasing preparation temperature until 90 °C. The maximum BET surface area and pore volume were 167.05 m^2·g^{-1} and 6.74 cm^3/g, respectively. Previous studies reported that low temperatures are conducive to the formation of Na$_2$O·nSiO$_2$ leachate to liquid silicon sol, but adverse to the reaction between leachate and Ca(OH)$_2$ suspension liquid. Fig. 7(b) shows the influence of

preparation time on the BET surface area and pore size of the silicate material. The maximum specific surface area and pore size were obtained at 1.5 h.

3-2. Influence of Si/Ca Molar Ratio and Stirring Rate on the Porous Silicate Material

The influence of Si/Ca molar ratio on the BET surface area and pore volume of the silicate material is shown in Fig. 7(c). The BET surface area considerably fluctuated with different Si/Ca molar ratios from 0.6 to 1.8. The BET surface area significantly increased when the Si/Ca molar ratio was increased from 0.6 to 0.8, and then slowly increased when the ratio reached 1.0. The maximum BET surface area and pore volume were 220.7 m^2·g^{-1} and 8.55 cm^3/g, respectively. The trend was similar to that of the pore volume. The BET surface area and pore volume of the silicate material sharply decreased when the Si/Ca molar ratio was increased from 1 to 1.8. Thus, the optimal Si/Ca molar ratio was confirmed at 1 : 1. Fig. 7(d) shows the influence of stirring rate on the BET surface area and pore volume under the following conditions: preparation temperature of 90 °C, preparation time of 1.5 h, and Si/Ca molar ratio of 1 : 1. As presented in Fig. 7(d), the BET surface area and pore volume of the porous silicate material exhibited an irregular change trend with increasing stirring rate. The results indicate that a suitable stirring rate favors the complete reaction between the leachate and the Ca(OH)$_2$ suspension liquid.
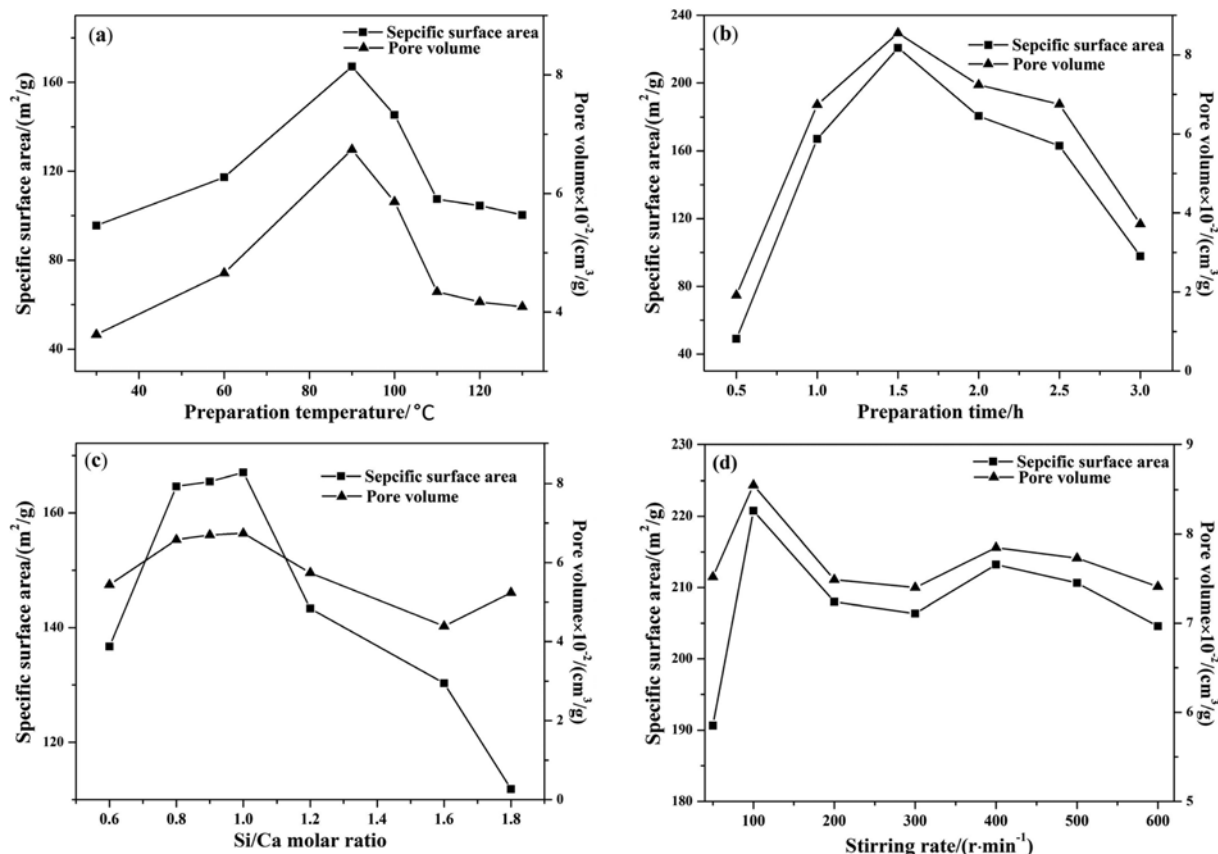

Fig. 7. (a) The influence of preparation temperature on the porous silicate materials; (b) the influence of preparation of preparation time on the porous silicate materials; (c) the influence of Si/Ca molar ratio on the porous silicate materials; (d) the influence of stirring rate on the porous silicate materials.

4. Characterization of the Porous Silicate Material

4-1. XRD Analysis

The XRD pattern of the porous silicate material is presented in Fig. 8. The XRD pattern generally presented a dispersed and unordered state. Only one evident and strong diffraction peak was observed at 29.24°, which may be attributed to calcite [24,25]. The
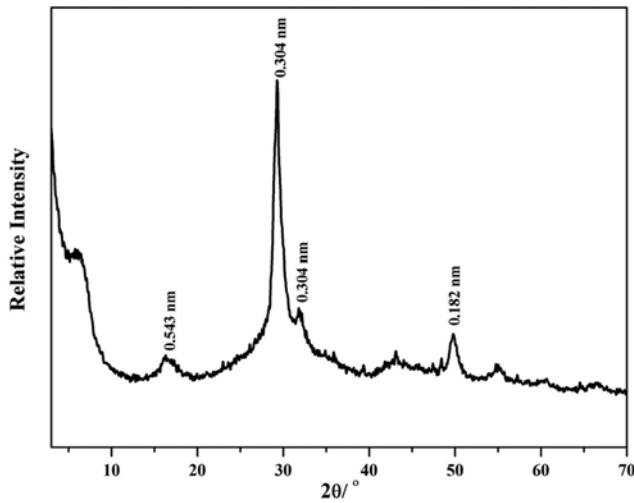
results indicate that the porous silicate material has an amorphous and unordered structure.

4-2. XPS Analysis

The XPS spectra of the porous material are shown in Fig. 9. There are two main bands observed at approximately 284.75 eV and 289.16 eV, which are the characteristic peaks position of C 1s
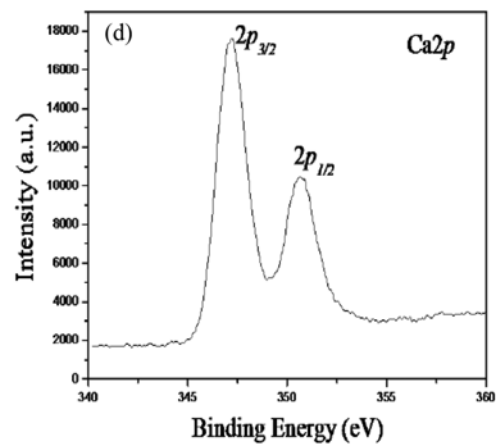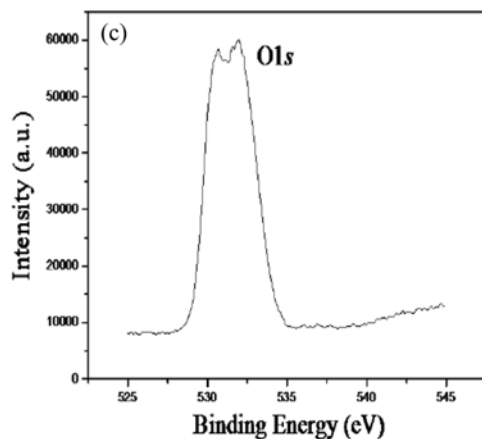

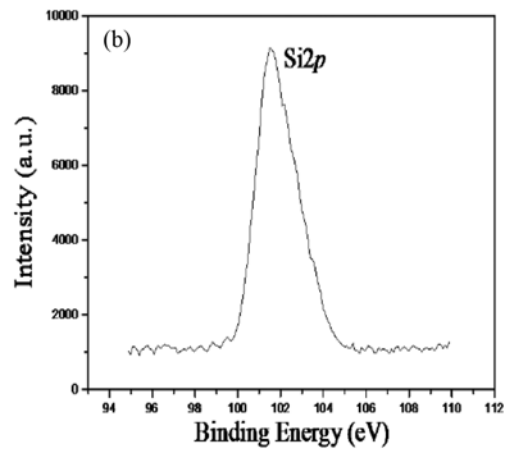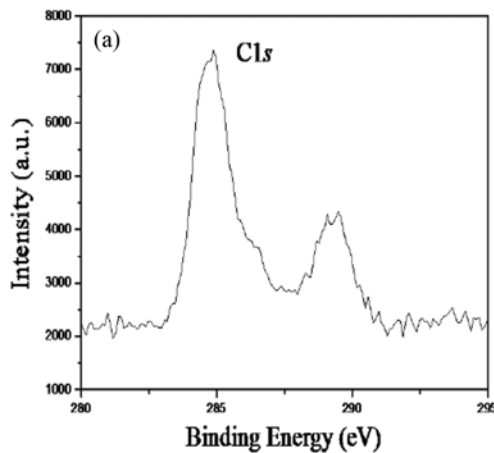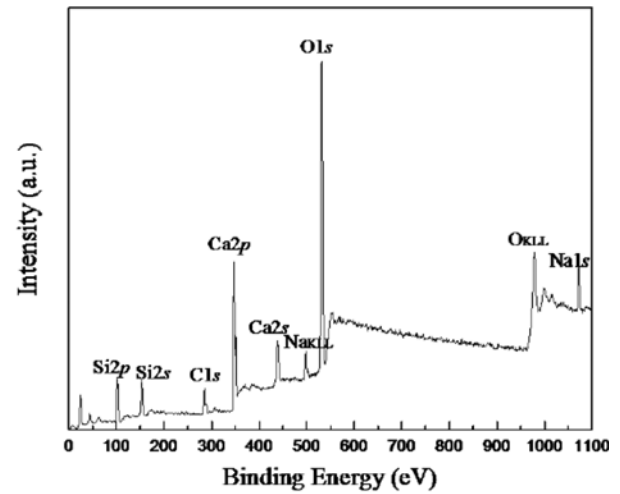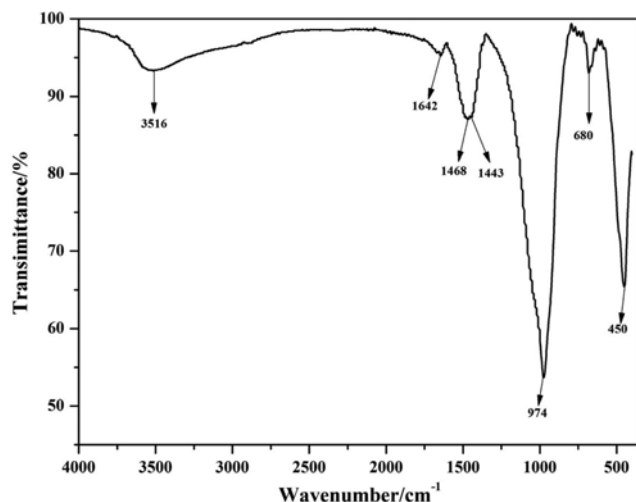Fig. 8. The XRD pattern of the porous silicate material.

Fig. 9. The XPS spectra of porous silicate material.

Fig. 10. The FT-IR spectroscopy of porous silicate material.

Fig. 11. The TG-DTG cures of porous silicate material.

Fig. 12. The N_2 adsorption and desorption isotherm of porous silicate material.

and assigned to a C^{4+} species. The band at 101.69 eV for Si 2p is attributed to Si^{4+} species, and the band at 538.48 eV for O 1s presents the existence of O^{2-} species [26]. These two bands at 346.68 and 350.28 eV correspond to the characteristic peaks of Ca $2p^{3/2}$ and Ca $2p^{1/2}$ for Ca^{2+} species [21]. The weak band at 1073.08 eV for Na 1s presents the existence of Na^+ species. The results indicate that the main chemical elements of porous silicate material are Ca, O, Si, C, and Na in the form Ca^{2+}, SiO_3^{2-}, CO_3^{2-}, and Na^+ ions, respectively.

4-3. FT-IR Analysis

The FT-IR spectrum of the porous silicate material is shown in Fig. 10. In the high wavenumber region (3,000-4,000 cm^{-1}), only one wide band with a moderate intensity can be observed at 3,516 cm^{-1}, which corresponds to the O-H stretching vibration mode. In the 1,500-2,000 cm^{-1} region, the band at 1,642 cm^{-1} is attributed to the O-H bending mode [27], and this band corresponds to the band at 3,516 cm^{-1}. The two bands at 1,468 cm^{-1} and 1,443 cm^{-1} are attributed to the anti-symmetric stretching vibration of CO_3^{2-} ion [25,28,29]. In the low wavenumber region (400-1,000 cm^{-1}), the band at 974 cm^{-1} is assigned to the anti-symmetric stretching vibration of Si-OH, and the band at 680 cm^{-1} presents the existence of SiO_3^{2-}. The band at 450 cm^{-1} is attributed to the bending vibration of Si-O-Si [30,31]. The results are in good agreement with the XRD data. The prepared silicate material presents porous and loose microstructure and higher special surface area relative to that of other hydrated silicates obtained in the literature [2,26,32-34], which led to that the prepared material presenting application advantages in adsorption and other fields.

4-4. TG-DTG Analysis

Thermal analysis reveals information about the thermal stability of materials. The TG-DTG curves of the porous silicate material are shown in Fig. 11. In the TG-DTG curves, the endothermic peak at 136 °C with a mass loss of 12.37% can be attributed to the desorption of the adsorption water of the porous silicate material. Meanwhile, the endothermic peak at 753 °C with a mass loss of 7.84% may be assigned to the decomposition of a small amount of calcium carbonate in the prepared material [35]. The TG-DSC
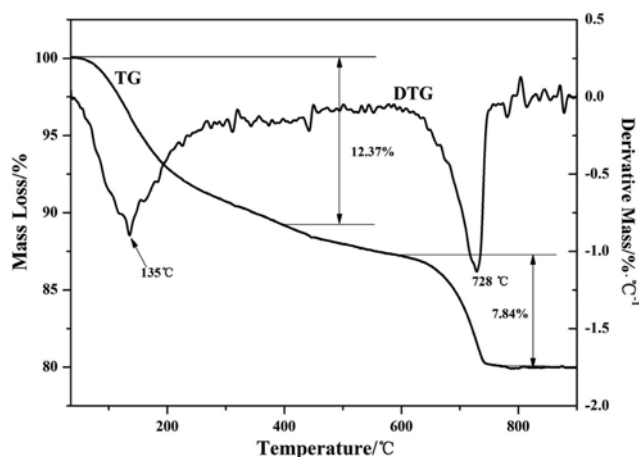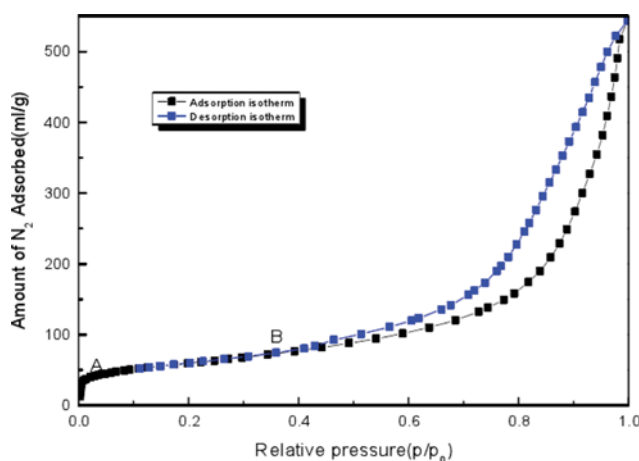
results agree with the XRD, XPS, and FT-IR data.

4-5. N_2 Adsorption and Desorption Isotherm Analysis

The N_2 adsorption and desorption isotherms of the porous silicate material are shown in Fig. 12. There is a large hysteresis loop in the isotherm at high relative pressure region (P/P_0=0.4-1.0). This result indicates that the porous silicate material has abundant mesopores and narrow pore size. A similar hysteresis loop can be observed at the low relative pressure region ($P/P_0 \leq 0.1$), which may be attributed to volume expansion or weak chemical adsorption [36]. The results indicate that the isotherm mode of the prepared material may be attributed to a combination of types III and IV and that the porous silicate material is a typical mesoporous material.

4-6. The Microstructure of Porous Silicate Material

SEM images of the porous silicate material are presented in Fig. 13. The microtopography of the porous silicate material presents lamellar and cellular structures, and a large number of pores with approximately 300 nm are distributed on the particle surface. The particles 5 μm to 10 μm in size present irregular shapes with a coarse surface. The overall microstructure of the particles exhibits a disorderly and amorphous structure, which agrees with the XRD data.
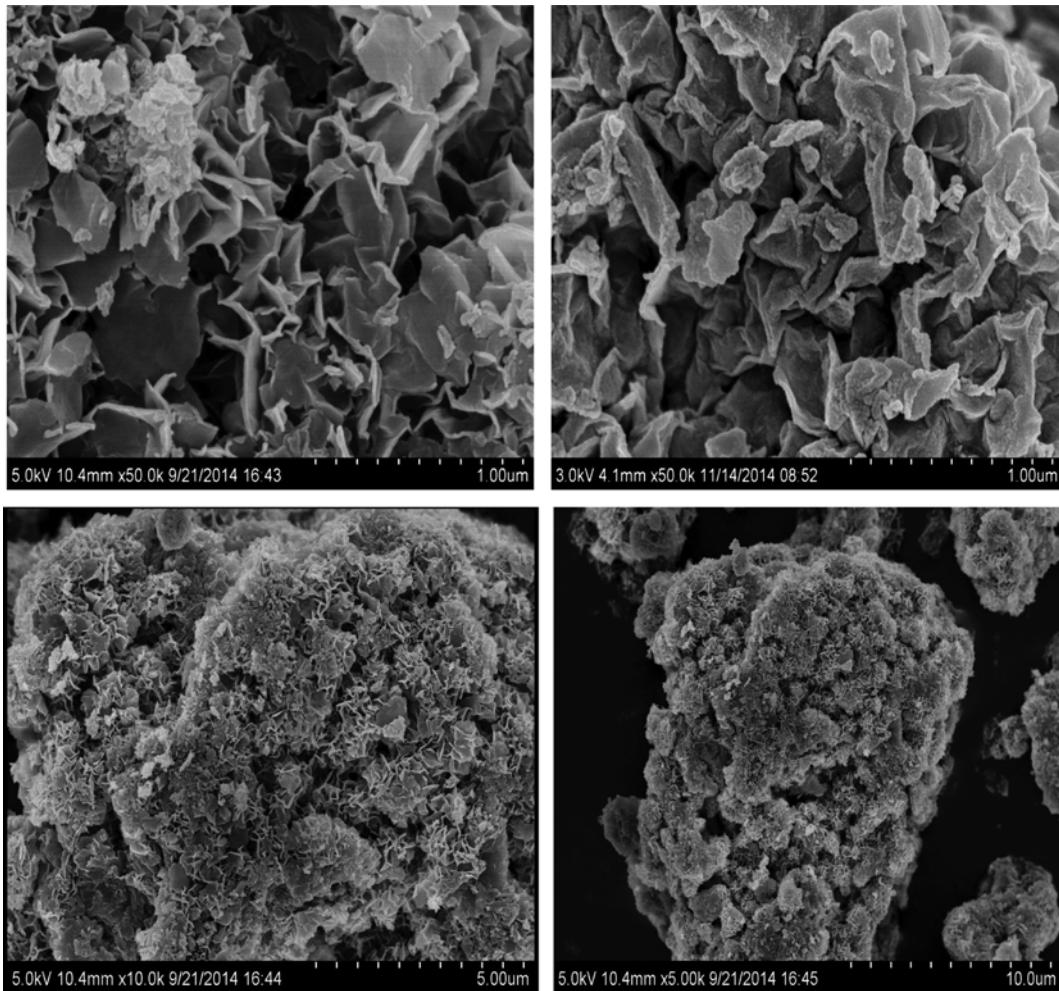
Fig. 13. The SEM images of porous silicate material.

5. Adsorption Thermal Dynamic Analysis of Porous Silicate Material for Formaldehyde

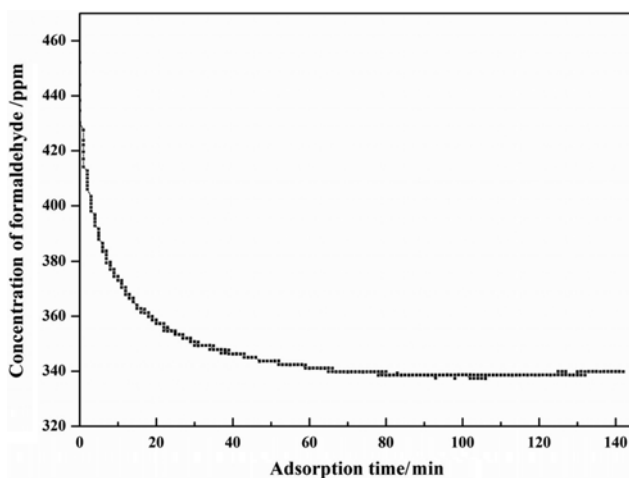The adsorption property of porous silicate material for formal-

Fig. 14. The adsorption curves of porous silicate material for formaldehyde.

dehyde was investigated by analyzing the experimental data based on the Langmuir isotherm equations. The adsorption curve of porous silicate material for formaldehyde is presented in Fig. 14. As seen, the concentration of formaldehyde in the equipment significantly decreased with increasing adsorption time before 30 min. Then, the adsorption rate of porous silicate material for formaldehyde gradually decreased, and reached saturated state when adsorption time was 140 min approximately. The Langmuir adsorption isotherm for monolayer adsorption on a homogeneous surface was successfully fitted to this adsorption process [26,37], and the saturated adsorption capacity reached $8.01\ mg \cdot g^{-1}$. The Langmuir constant K_L was $21.31\ L \cdot g^{-1}$, and the adsorption Gibbs free energy change was $-7.58\ kJ \cdot mol^{-1}$ based on the van't Hoff equation. The absolute value of adsorption Gibbs free energy change was lower than $20\ kJ \cdot mol^{-1}$, which indicated that the adsorption was assigned to physical adsorption. The comparison results on the formaldehyde sorption capacity of other adsorption materials are shown in Table 2. The saturated adsorption capacity and rate of adsorption for prepared silicate material is $8.01\ mg \cdot g^{-1}$ and $0.280\ mg \cdot g^{-1} \cdot min^{-1}$ respectively, which presents an advantage than that of other silicate material and commercial adsorbent. From the above result, the prepared silicate material presents a strong re-

Table 2. The comparison results on the formaldehyde sorption capacity of other adsorption materials

Adsorbent	Saturated adsorption capacity (mg·g^{-1})	Rate of adsorption (mg·g^{-1}·min^{-1})
Diatomite	0.408	0.024
Sodium bentonite	2.176	0.017
Calcium bentonite	2.079	0.027
Commercially Adsorbent	5.607	0.089
Porous silicate material	8.01	0.280

moval capability to formaldehyde. Based on above data, the prepared porous silicate material could be used as for adsorbing volatile organic compound and decontaminating indoor air environment, including formaldehyde, benzene, methylbenzene, and other pollutants.

CONCLUSIONS

A novel porous silicate material from silica fume was successfully prepared and characterized by a series measurement methods. The following main conclusions can be drawn.

(1) The maximum SiO_3^{2-} extraction yield of 90.69% was obtained under the following conditions: reaction temperature of 120 °C, reaction time of 120 min, NaOH concentration of 15%, and alkali to SiO_2 molar ratio of 2. The porous silicate material was readily prepared from the leaching SiO_3^{2-} under the following conditions: preparation temperature of 90 °C, preparation time of 1.5 h, Si/Ca molar ratio of 1 : 1, and the stirring rate of 100 r/min.

(2) The BET surface area and pore size of the porous silicate material were 220.7 m^2·g^{-1} and 8.55 cm^3/g, respectively. The porous silicate material was mainly composed of Si, Ca, O, C, and Na, in the form of Ca^{2+}, SiO_3^{2-}, CO_3^{2-} and Na^+ ions, respectively, which agrees with the XRD, TG-DSC, and FT-IR data. The N_2 adsorption-desorption isotherm mode indicates that the porous silicate material is a typical mesoporous material. The porous silicate material exhibited a large number of developed pores and fibrous and flake network structure with an excellent thermal stability.

(3) The porous silicate material presented efficiency for the removal of formaldehyde: it showed a formaldehyde adsorption capacity of 8.01 mg/g for 140 min at 25 °C.

ACKNOWLEDGEMENT

REFERENCES

1. X. Li, A. H. Korayem, C. Li, Y. Liu, H. He, J. G. Sanjayan and W. H. Duan, *Constr Build Mater.*, 123 (2016).
2. Z. Jinliang, G. Zhancheng, Z. Xin and T. Huiqing, *Chin. J. Pro. Eng.*, 12 (2012).
3. C. Zhou, C. Yan, J. Zhao, H. Wang, Q. Zhou and W. Luo, *J. Taiwan. Inst. Chem. E*, 62 (2016).
4. H. Ji, Z. Huang, K. Chen, W. Li, Y. Gao, M. Fang, Y. Liu and X. Wu, *Powder. Technol.*, 252 (2014).
5. M. Mastali and A. Dalvand, *Constr. Build. Mater.*, 125 (2016).
6. M. Fakhri and F. Saberi. K, *J. Clean. Prod.*, 129 (2016).
7. A. A. Ramezanianpour, Springer Berlin Heidelberg, 193 (2014).
8. L. Lijuan, L. Tielong and J. Zhaohui, *Chin. J. Enviro. Eng.*, 4 (2010).
9. V. Lilkov, O. Petrov, D. Kovacheva, I. Rostovsky, Y. Tzvetanova, V. Petkova and N. Petrova, *Constr. Build. Mater.*, 124 (2016).
10. F. N. Okoye, J. Durgaprasad and N. B. Singh, *Ceram. Int.*, 42 (2016).
11. H. Gaoping and X. Weidong, *Henan. Chem. Ind.*, 07 (2006).
12. Z. Deyi, F. Huixia, L. Heming, W. Yi, C. Xuefu and W. Yanjun, *Chin. Non-Metallic. Miner. Ind.*, 5 (2009).
13. W. Li, X. Ping, Y. Xu, H. Li, Z. Yi and Y. Tang, *Concrete.*, 6 (2011).
14. H. Zhu, Shandong University of Science and Technology Doctor Degree (2009).
15. H, Hai, Y. Zhang, Y. Zhang, J. Sun and Z. Hao, *Chin. J. Enviro. Eng.*, 11 (2017).
16. J. Zhang, Z. Guo, X. Z and H. T, *Chinese J. Environ. Eng.*, **12**, 2 (2012).
17. Azouaoua N, Sadaou Z, Djaafri A, et al., *J. Hazar. Mater.*, 184 (2010).
18. Anirudhan T S, RadhakrishLnan P G, *Thermodynamics.*, 40 (2008).
19. I. Langmuir, *J. Am. Chem. Soc.*, **40**, 1361 (1918).
20. S. Onisei, Y. Pontikes, T. V. Gerven, G. N. Angelopoulos, T. Velea, V. Predica and P. Moldovan, *J. Hazard. Mater.*, 101 (2012).
21. Y. Gao, H. Huang, W. Tang, X. Liu, X. Yang and J. Zhang, *Micropor. Mesopor. Mater.*, 217 (2015).
22. G. J. Maximo, A. J. A. Meirelles and E. A. C. Batista, *Fluid Phase Equilibr.*, 299 (2010).
23. R. Wang, Y. Zhai, Z. Ning and P. Ma, *T Nonferr Metal Soc.*, 24 (2014).
24. R. R. Yadav, S. N. Mudliar, A. Y. Shekh, A. B. Fulke, S. S. Devi, K. Krishnamurthi, A. Juwarkar and T. Chakrabarti, *Process Biochem.*, 47 (2012).
25. J. Sun, Z. Wu, H. Cheng, Z. Zhang and R. L. Frost, *Spectro. Act. Part A: Mole. and Biomo. Spec.*, 117 (2014).
26. X. Yang, X. Liu, W. Tang, Y. Gao, H. Ni and J. Zhang, *Korean J. Chem. Eng.*, **34**, 3 (2017).
27. L. Li, Y. Zhang, Y. Zhang, J. Sun and Z. Hao, *J. Therm. Anal. Calorim.* (2016), DOI:10.1007/s10973-016-5711-4.
28. H. Zaitan, D. Bianchi, O. Achak and T. Chafik, *J. Hazard. Mater.*, 153 (2008).
29. A. Meiszterics, L. Rosta, H. Peterlik, J. Rohonczy, S. Kubuki, P. Henits and K. Sinko, *J. Phys. Chem. A*, 114 (2010).
30. Y. Zhang, Q. Liu, Z. Wu, Q. Zheng and H. Cheng, *J. Therm. Anal. Calorim.* (2012), DOI:10.1007/s10973-011-2038-z.
31. Y. Zhang, Q. Liu, Z. Wu and Y. Zhang, *J. Therm. Anal. Calorim.* (2015), DOI:10.1007/s10973-015-4652-7.
32. P. Xiaoqin, Z. Huixing, J. Xiaohua and X. Guowei, *J. Chin. Cer. Soc.*, 36 (2008).
33. P. Xiaoqin, H. Fang, Z. Le, Qi. Xuejun and T. Yuanyan, *J. Southwest Jiaotong Univ.*, 44 (2009).
34. H. Jilin, L. Xin, X. Hanning, Y. Zhishu and P. Yangxi, *Inorgan*

Chem. Ind., 41 (2009).

35. H. Jingnan, S. Junmin, X. Xuebin, Y. Huibin and L. Yungai, *Bulle. Chin. Cer. Soc.*, 35 (2016).

36. W. Tang, H. Huang, Y. Gao, X. Liu, X. Yang, H. Ni and J. Zhang, *Mater. Des.*, 88 (2015).

37. B. Özkaya, *J. Hazard. Mater.*, **B 129**, 158 (2006).